Online ISSN 2755-2500
Print ISSN 2755-2608
Volume 3 Number 3
May 2025
rsc.li/icm

Industrial Chemistry & Materials

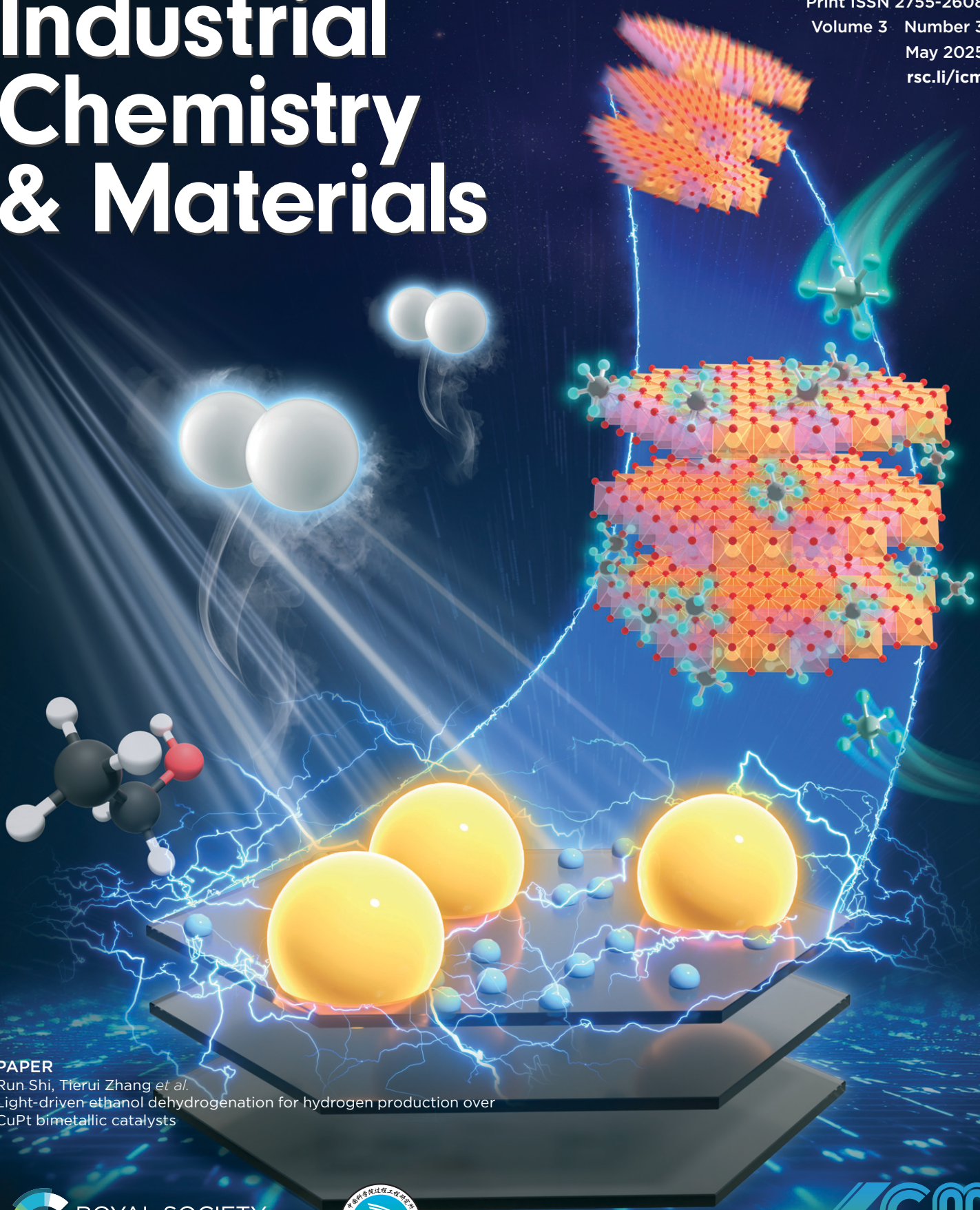

PAPER
Run Shi, Tierui Zhang *et al.*
Light-driven ethanol dehydrogenation for hydrogen production over CuPt bimetallic catalysts

ROYAL SOCIETY OF CHEMISTRY

Industrial Chemistry & Materials

Industrial Chemistry & Materials

ROYAL SOCIETY OF CHEMISTRY

PAPER

View Article Online
View Journal | View Issue

Cite this: *Ind. Chem. Mater.*, 2025, **3**, 332

Light-driven ethanol dehydrogenation for hydrogen production over CuPt bimetallic catalysts†

Shihao Du,[ab] Run Shi,[*a] Jiaqi Zhao,[a] Pu Wang,[ab] Jinhu Wang,[ab] Zhenhua Li,[a] Peng Miao,[ab] Qianqian Shang,[c] Chi Duan[ab] and Tierui Zhang[*ab]

Received 22nd December 2024,
Accepted 14th March 2025

DOI: 10.1039/d4im00158c

rsc.li/icm

The ethanol dehydrogenation (ED) reaction is considered a sustainable pathway for hydrogen production. However, the ED reaction is energy-intensive as it requires high temperatures. Here, we report a layered double hydroxide-derived catalyst composed of CuPt bimetallic nanoparticles for efficient light-driven ED reaction without additional thermal energy input, achieving a hydrogen production rate of 136.9 μmol g^{-1} s^{-1}. This rate is 1.4 times higher than that achieved at the same temperature in the dark. Experimental results and theoretical simulations suggest that the localized surface plasmon resonance (LSPR) effect of Cu reduces the apparent activation energy of the light-driven ED reaction. The presence of Pt nanoparticles around Cu enhances the LSPR effect, thereby significantly increasing the hydrogen production efficiency.

Keywords: Light-driven; Ethanol dehydrogenation; Hydrogen production; LSPR.

1 Introduction

Hydrogen is a crucial clean energy source with a high calorific value (120 MJ kg^{-1}), and its combustion produces only water.[1,2] Meanwhile, hydrogen also plays a vital role in industrial manufacturing, ammonia production, and methanol production.[3,4] Currently, the primary source of hydrogen is the reforming of fossil fuels such as methane, which results in significant greenhouse gas emissions.[5–7] Ethanol dehydrogenation (ED, $CH_3CH_2OH \rightarrow CH_3CHO + H_2$, ΔH = 68 kJ mol^{-1}) is considered a promising alternative process for hydrogen production.[8–12] Ethanol, the reactant, can be produced in large quantities from biomass, and the by-product mainly contains acetaldehyde, an important chemical raw material.[8] Additionally, storing hydrogen gas in ethanol as a liquid carrier and releasing it through a catalytic ED process can significantly reduce the storage and transportation costs associated with hydrogen energy.[13]

Because the ED reaction is endothermic, it requires high temperatures (250–350 °C), leading to substantial energy consumption. Consequently, the ED reaction driven by sustainable energy has become a research hotspot.[10,14] Recently, photocatalysis, driven by either artificial light sources or sunlight, has gained widespread attention as a potential alternative to conventional thermocatalysis in reactions such as dry reforming of methane,[15–17] CO_2 reduction,[18,19] water-gas shift reaction,[20] and Fischer–Tropsch synthesis.[21] The synergistic effect between photoinduced charge carriers and the photothermal effect typically result in higher reaction efficiency compared to dark conditions at the same temperatures.[6,21]

Copper-based nanomaterials have been widely studied for thermocatalytic ED reactions due to their robust ability for C–H and O–H bond activation and weak activity in C–C bond cleavage.[11,22–27] However, they face challenges related to low catalytic activity and stability. Plasmonic nanostructures (such as Au, Ag, and Cu), which can efficiently harness and convert solar energy into chemical energy, have emerged as promising photocatalysts.[7,28–31] Cu has garnered attention for plasmonic catalysis due to its favorable localized surface plasmon resonance (LSPR) effect in the visible light region and exceptional photothermal properties.[6,7,32] Additionally, introducing secondary metals around plasmonic nanoparticles (NPs) is an effective strategy to enhance the LSPR effect and reaction efficiency.[33–35] For instance, Emiliano Cortés reported a bimetallic supercrystal composed

[a] *Key Laboratory of Photochemical Conversion and Optoelectronic Materials, Technical Institute of Physics and Chemistry, Chinese Academy of Sciences, Beijing 100190, China. E-mail: shirun@mail.ipc.ac.cn, tierui@mail.ipc.ac.cn*
[b] *Center of Materials Science and Optoelectronics Engineering, University of Chinese Academy of Sciences, Beijing 100049, China*
[c] *College of Chemistry and Chemical Engineering, Liaocheng University, Liaocheng 252000, China*

† Electronic supplementary information (ESI) available. See DOI: https://doi.org/10.1039/d4im00158c

of Au and Pt NPs that exhibited an H_2 production rate of 139 mmol g^{-1} h^{-1} *via* formic acid dehydrogenation under visible light illumination.[36] Therefore, Cu and Cu-based bimetallic catalysts are possible candidates for light-driven ED reactions with enhanced activity under mild reaction conditions.

Herein, we synthesized layered double hydroxide (LDH)-derived CuPt bimetallic NPs (LD-CuPt) for light-driven ED reaction. The LD-CuPt exhibited an H_2 production rate of 136.9 μmol g^{-1} s^{-1} under ultraviolet-visible (UV-visible) light illumination without external heating, which is higher than that of the same catalyst at the same temperature in the dark (99.9 μmol g^{-1} s^{-1}). Meanwhile, the LD-CuPt exhibited 5 h of continuous stability and 0.78% apparent photoactivation efficiency (PAE). The presence of Pt NPs around Cu NPs under illumination effectively reduced the apparent activation energy to 51.8 kJ mol^{-1}. Monochromatic light experiments revealed that the elevated H_2 production activity under UV-visible irradiation was due to the LSPR effect of the Cu NPs. Finite difference time domain (FDTD) calculation results further proved that the surrounding Pt NPs enhanced the LSPR effect of Cu.

2 Results and discussion

2.1 Structural characterization

LD-CuPt was synthesized through the following process (Fig. 1a). The first step is to synthesize CuAl-LDH nanosheets as precursors using a coprecipitation method. Subsequently, CuAl-LDH was immersed in $H_2PtCl_6{\cdot}6H_2O$ solution to obtain Pt/CuAl-LDH. Finally, LD-CuPt was prepared by calcining Pt/

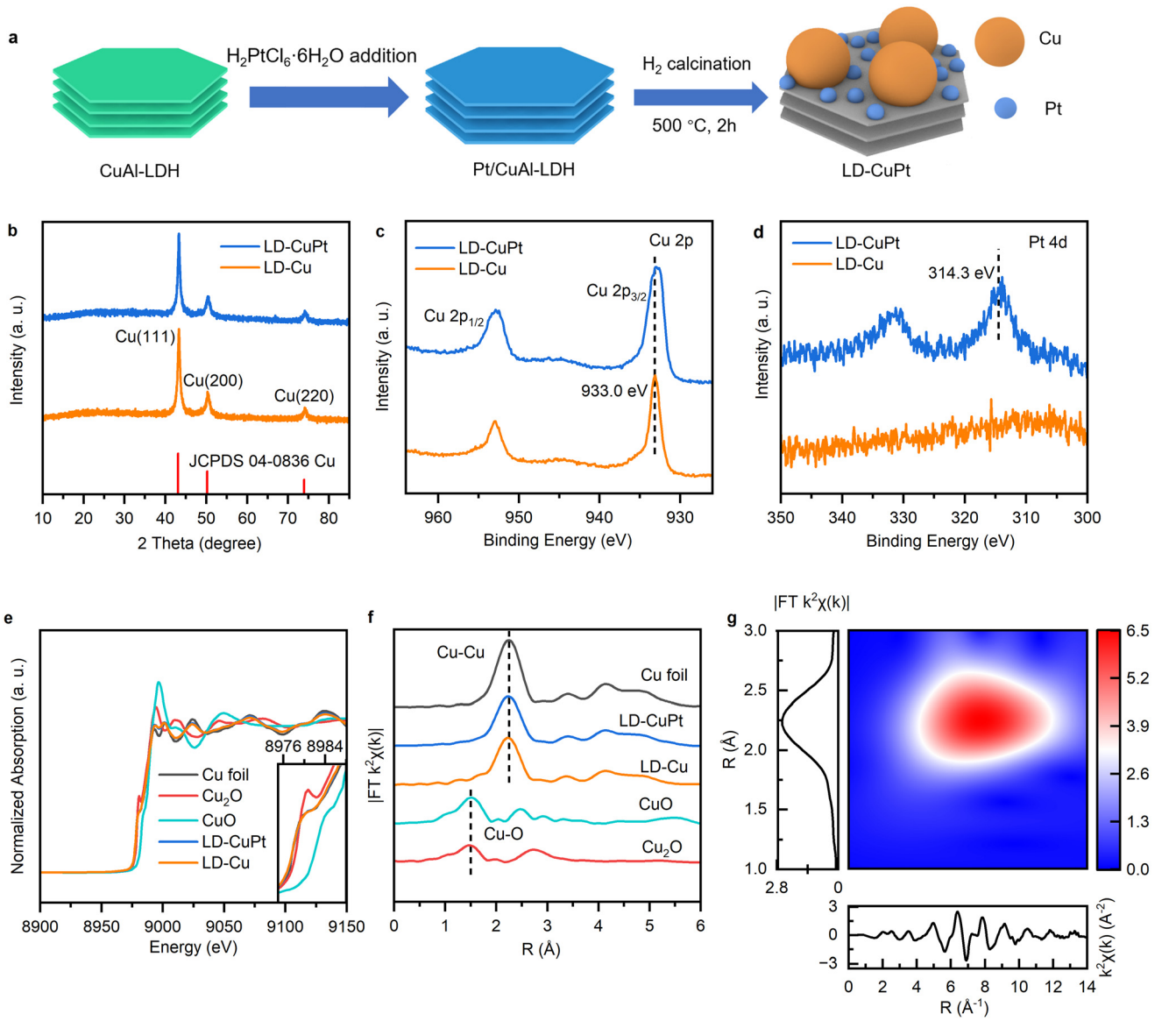

Fig. 1 (a) Schematic diagram of the synthesis of LD-CuPt. (b) XRD patterns of LD-CuPt, and LD-Cu. (c) XPS Cu 2p spectra of LD-CuPt and LD-Cu. (d) XPS Pt 4d spectra of LD-CuPt, and LD-Cu, (e) Cu K-edge X-ray absorption near-edge structure for LD-CuPt, LD-Cu, and reference samples. (f) Cu K-edge EXAFS spectra of LD-CuPt, LD-Cu and reference samples. (g) Wavelet transform for the k^2-weighted EXAFS signal of LD-CuPt.

CuAl-LDH under a hydrogen atmosphere at 500 °C. The Cu and Pt contents in catalysts were measured by inductively coupled plasma-optical emission spectroscopy (ICP-OES, Table S1†). We also prepared other second metal-modified catalysts (denoted as LD-CuM, M = Ag, Au, Ir, and Pd) using methods similar to those used to prepare LD-CuPt.

The structure of the as-obtained samples was initially examined by powder X-ray diffraction (XRD) analysis. The XRD patterns of CuAl-LDH and Pt/CuAl-LDH showed peaks at 11.6°, 22.7°, and 35.5° (Fig. S1†), corresponding to the (003), (006), and (009) planes of CuAl-LDH (JCPDS 46-0099). The LD-CuPt catalyst exhibited clear diffraction peaks at 43.3°, 50.4°, and 74.1° (Fig. 1b), corresponding to the (111), (200), and (220) planes of metallic Cu (JCPDS 04-0836). However, no peaks related to Al were detected. No diffraction peaks related to Pt were detected in LD-CuPt, which may be due to the low content and high dispersion of Pt. The XRD pattern of the LDH-derived Cu NPs (LD-Cu) without Pt decoration also showed peaks indexed to metallic Cu (Fig. 1b).

To further understand the chemical composition and electronic states of LD-CuPt and LD-Cu, X-ray photoelectron spectroscopy (XPS) was performed. The Cu 2p spectra in Fig. 1c unveiled the existence of Cu(0) (933.0 eV, $2p_{3/2}$) for LD-CuPt and LD-Cu.[37] Considering the overlap of the signals between Al 2p and Pt 4f at ~73 eV, we focused on the signals of Pt 4d orbitals near the binding energy of ~314 eV.[38,39] LD-Cu had no Pt 4d signal (Fig. 1d), while LD-CuPt presented a peak at 314.3 eV corresponding to Pt(0). Cu K-edge X-ray absorption spectroscopy (XAS) was then performed. Cu foil, Cu2O, and CuO were used as reference materials. The Cu K-edge near-edge features of LD-CuPt and LD-Cu (Fig. 1e) were similar to those of the Cu foil, confirming the presence of metallic Cu in LD-CuPt and LD-Cu. This conclusion was further confirmed by Cu K-edge extended X-ray absorption fine structure (EXAFS) results. As shown in Fig. 1f, the EXAFS data for LD-CuPt and LD-Cu showed a Cu–Cu coordination feature at 2.2 Å in *R*-space. The Cu K-edge wavelet transform (WT) of LD-CuPt (Fig. 1g) showed a sole contour peak with a maximum strength of approximately 8.0 $Å^{-1}$, which was close to that of Cu foil (Fig. S2†).

The morphologies of CuAl-LDH, Pt/CuAl-LDH, and LD-CuPt were studied by transmission electron microscopy (TEM). CuAl-LDH and Pt/CuAl-LDH were both nanosheets with a lateral size of 200–500 nm (Fig. S3 and S4†). LD-CuPt consists of nanosheet-supported NPs with sizes of 30–50 nm (Fig. 2a). The diameters of Cu NPs in the LD-Cu were similar to those in LD-CuPt (Fig. S5†). The high-resolution TEM (HRTEM) image and corresponding fast Fourier transform revealed lattice fringes of 0.23 nm, 0.21 nm, and 0.18 nm, corresponding to the Pt (111), Cu (111), and Cu (200) plane,

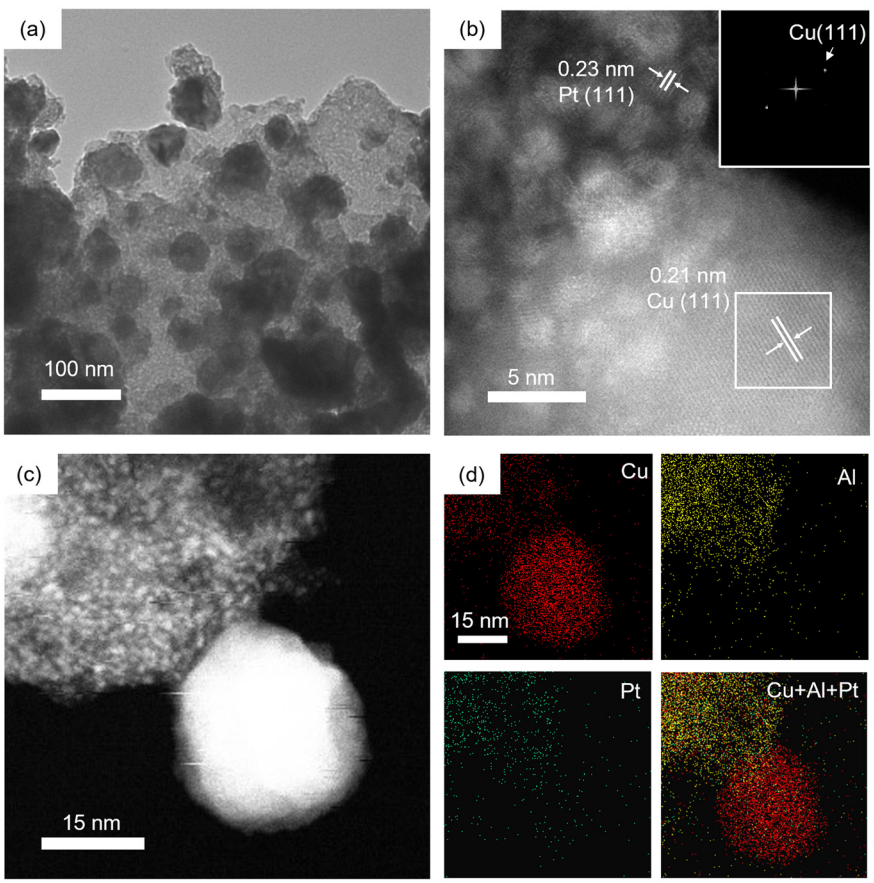

Fig. 2 (a) TEM image, (b) HRTEM image (inset is the fast Fourier transform of the boxed region), (c) HAADF-STEM image, and (d) EDS element maps of LD-CuPt.

respectively (Fig. 2b and S6†). It was also shown that Pt NPs with particle sizes of 1–3 nm were dispersed around Cu NPs. Fig. 2c and d display a high angle annular dark field scanning transmission electron microscopy (HAADF-STEM) image and corresponding element maps of LD-CuPt. Results confirmed the presence of highly dispersed CuPt bimetallic NPs supported on amorphous aluminum oxide.

2.2 Light-driven ED for hydrogen production.

Light-driven ED tests were carried out using a homemade flowing photoreactor under UV-visible irradiation (Fig. S7†). First, the influence of different second metals in LD-CuM was studied (Fig. 3a). The LD-CuPt catalyst exhibited an H_2 production rate of 136.9 μmol g^{-1} s^{-1}, 2.1 times higher than that of the LD-Cu catalyst (64.0 μmol g^{-1} s^{-1}) under the same reaction conditions. The performance is better than that of most photocatalysts and thermocatalysts reported to date (Table S2†). LD-CuPt and LD-Cu have similar specific surface areas, and the H_2 production rate of LD-CuPt after specific surface area normalization was also higher than that of LD-Cu (Fig. S8†).[40,41] This indicates that the improvement in H_2 production rates of LD-CuPt compared to LD-Cu is not only due to an increase in surface area but also other factors. LD-CuAu, LD-CuIr, and LD-CuPd catalysts showed slightly improved H_2 production rates of 77.6, 102.9, and 98.7 μmol g^{-1} s^{-1} compared to LD-Cu. Meanwhile, the H_2 production rate of LD-CuAg (38.0 μmol g^{-1} s^{-1}) was lower than that of LD-Cu. Both Pt/Al_2O_3 (Pt loaded on commercial Al_2O_3) and Pt/CuAl-LDH produced only a small amount of H_2. These results indicated that metallic Cu is the active phase for the ED reaction, while Pt as the second metal in the CuPt bimetallic catalyst possibly plays a significant role in enhancing the ED reaction kinetics on Cu NPs. The loading amount of Pt also affected the performance of the catalyst (Fig. 3b). The production rate of H_2 increased with the Pt loadings from 0 to 5 wt% and reached a plateau by further raising the Pt loading to 7 wt%. Therefore, 5 wt% LD-CuPt showed the highest H_2 production rate and was used for subsequent investigations.

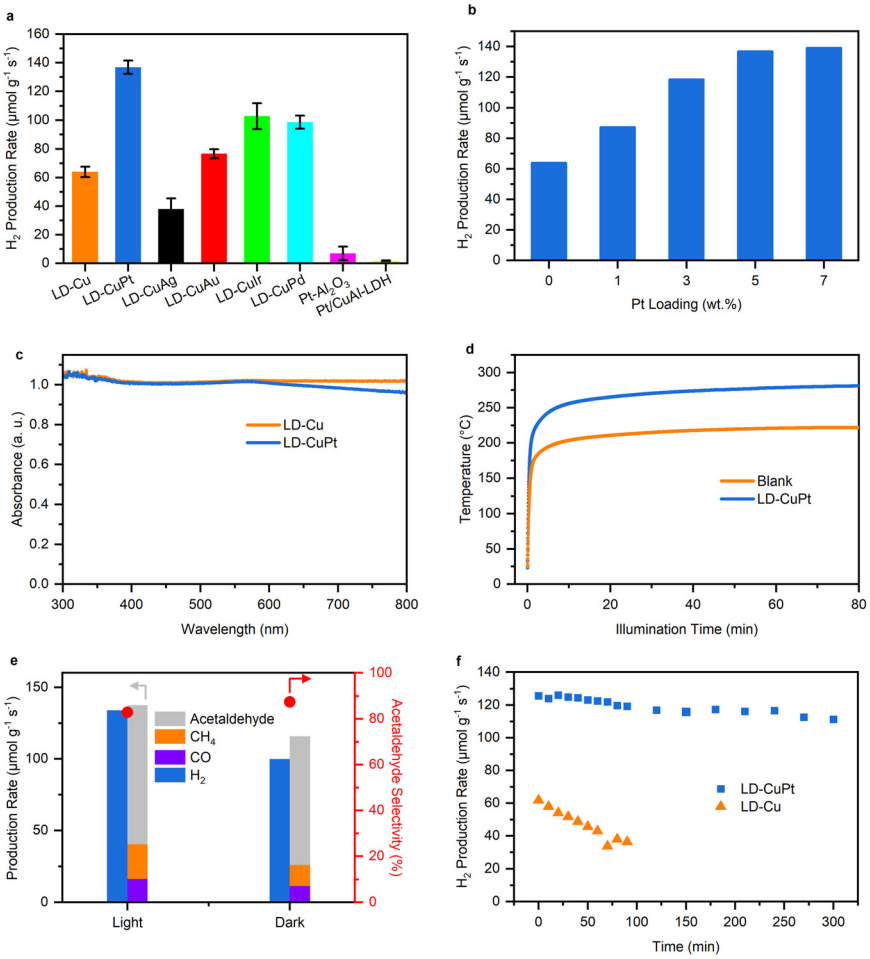

Fig. 3 (a) H_2 production rates over LD-Cu, LD-CuM, and control samples. (b) H_2 production rates of LD-CuPt as a function of Pt loading amount. (c) UV-visible absorption spectra of LD-CuPt and LD-Cu. (d) Surface temperature of LD-CuPt and blank under UV-visible irradiation (light intensity = 1.1 W cm^{-2}). (e) Production rates and acetaldehyde selectivity of LD-CuPt under light and dark conditions at 280 °C. (f) Light-driven ED reaction stability test of LD-CuPt and LD-Cu. Error bars represent standard deviations obtained from three independent measurements.

Both LD-CuPt and LD-Cu catalysts exhibited strong light absorption across the UV-visible region, highlighting their excellent photothermal properties (Fig. 3c). Subsequently, the time-dependent surface temperature of LD-CuPt under illumination was measured (see section 4.6 for experimental details).[42,43] Under 1.1 W cm^{-2} illumination, the temperature rose rapidly at first and then stabilized after approximately 9 minutes of irradiation, with a final temperature of about 280 °C. The excellent photothermal effect of LD-CuPt results in an increased local temperature during the endothermic ED reaction, thereby enabling it to overcome the energy barriers of ethanol activation and conversion, thus accelerating the overall reaction rate.[14,44,45] Under identical irradiation conditions, the surface temperature of the glass fiber membrane without a catalyst (denoted as blank) reached only 220 °C (Fig. 3d). The H_2 production rate increased with increasing space velocity in the low space velocity region (10–50 mL min^{-1}) and then remained nearly unchanged with further increases in space velocity (Fig. S9†). The apparent PAE of LD-CuPt was then calculated to reveal the light energy utilization efficiency for activating the ED reaction.[46] The apparent PAE increased with the light intensity and reached a maximum of 0.78% at 1.1 W cm^{-2} (Fig. S10†).

We then evaluated the selectivity of carbon-containing products over LD-CuPt. As shown in Fig. 3e, under light conditions, the selectivity of acetaldehyde reached 82.8%. The other by-products were CO and CH_4, with production rates of 16.2 and 24.1 μmol g^{-1} s^{-1}, respectively. Under dark conditions at the same reaction temperature, the H_2 production rate decreased to 99.9 μmol g^{-1} s^{-1}, and the selectivity of acetaldehyde was almost the same as that under light conditions. In addition, the LD-CuPt catalyst showed

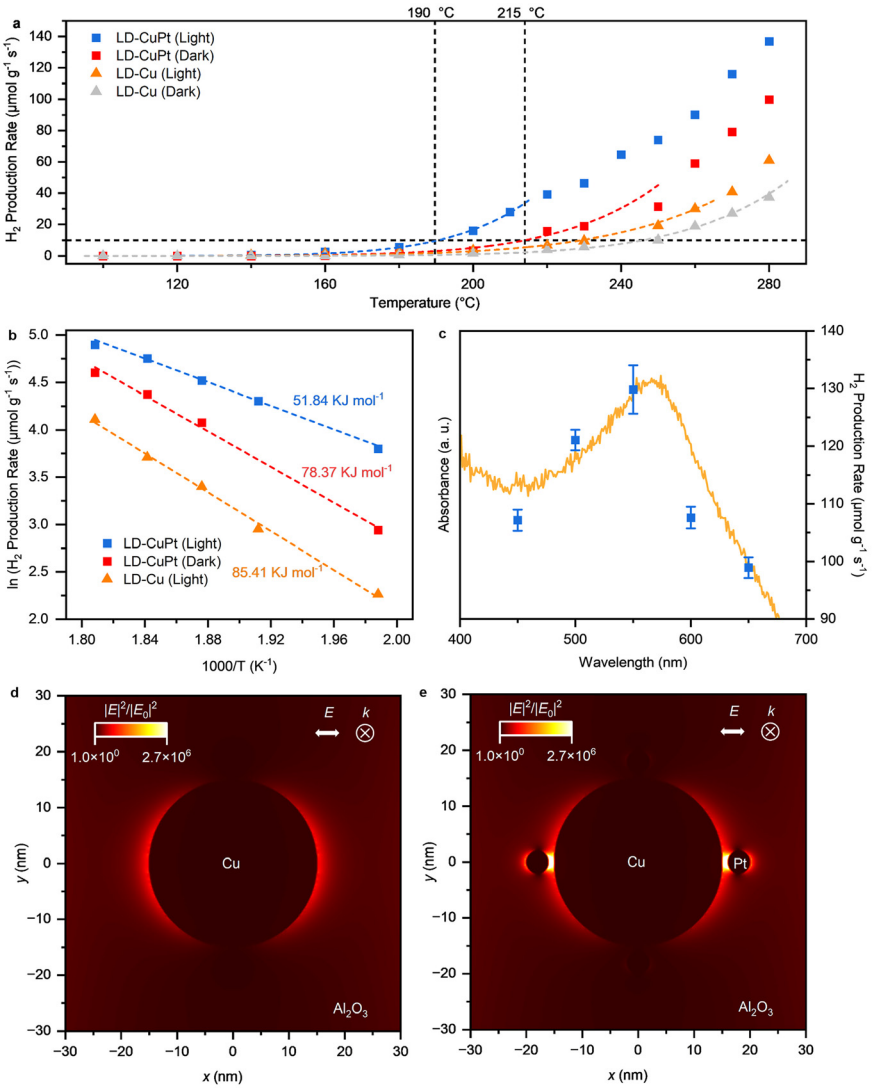

Fig. 4 (a) H_2 production rates of LD-CuPt and LD-Cu under light and dark conditions plotted against reaction temperatures. (b) H_2 production Arrhenius plots over LD-CuPt and LD-Cu. (c) UV-visible absorption spectra of LD-CuPt and corresponding H_2 production rates at 280 °C under monochromatic light irradiation. FDTD simulation of (d) a Cu NP and (e) a Cu NP surrounded by four Pt NPs. The colored bar shows the electromagnetic field intensity normalized by the light source intensity ($|E|^2/|E_0|^2$). Error bars represent standard deviations obtained from three independent measurements.

almost no performance degradation within 5 hours of irradiation, while the LD-Cu catalyst showed 40% performance degradation after 1.5 hours, indicating that the introduction of Pt also improved the stability of the catalyst (Fig. 3f). XRD and TEM of LD-CuPt after reactions were consistent with those of the as-prepared sample, suggesting its superior stability (Fig. S11 and S12†).

2.3 Mechanistic investigations

Fig. 4a shows H_2 production rates from both light-driven and thermo-driven ED reactions at different reaction temperatures over LD-CuPt and LD-Cu. At the same temperature, the H_2 production rates of LD-CuPt under light conditions are higher than those under dark conditions. In addition, the onset reaction temperature (H_2 production rate = 10 μmol g^{-1} s^{-1}) of LD-CuPt was reduced by approximately 25 °C from 215 °C in the dark to 190 °C under light irradiation. For light conditions at 230 °C, the H_2 production rate of LD-CuPt (46.4 μmol g^{-1} s^{-1}) was nearly 2.4 times higher than the reaction rate in the dark (18.9 μmol g^{-1} s^{-1}). For cycling experiments (0.5 h for each cycle, 10 cycles in total), LD-CuPt showed stable H_2 production in both light and dark conditions, and the light-driven H_2 production rate was consistently better than that in the dark (Fig. S13†). As shown in the Arrhenius plots in Fig. 4b, the apparent activation energy (E_a) over LD-CuPt was reduced from 78.3 kJ mol^{-1} in the dark to 51.8 kJ mol^{-1} under illumination (Fig. 4b).

The above results demonstrate the function of incident light in facilitating the reaction kinetics beyond a photothermal heating effect[7] and further reveal the function of Pt as the second metal in enhancing the H_2 production rate and lowering the E_a. We further tested the H_2 production rate of LD-CuPt under different monochromatic light irradiation (Fig. 4c and S14†) at 280 °C. The H_2 production rate peaked at 550 nm, which showed a similar trend to the LSPR feature of Cu, indicating that the LSPR excitation of the Cu NPs contributed to the enhanced H_2 production activity.[47]

To gain deeper insights into the LSPR effect in the CuPt bimetallic catalyst, light-induced local electromagnetic fields around a single Cu NP and a Cu NP surrounded by four Pt NPs on an Al_2O_3 nanosheet were simulated using the FDTD method (Fig. 4d and e and S15†). The electromagnetic field of the Cu NP surrounded by Pt NPs was higher than that of a single Cu NP. The electromagnetic field at the interparticle gap between Cu and Pt NPs was much larger than that at other positions. These high-intensity electromagnetic field hot spots suggest that the surrounding Pt NPs enhanced the LSPR effect of Cu NPs, thereby promoting the light-driven ED reaction kinetics and resulting in enhanced H_2 production efficiency.[48–50]

3 Conclusion

In summary, we have reported an LDH-derived CuPt bimetallic catalyst for light-driven ED reaction with high hydrogen production rates. The optimized LD-CuPt catalyst shows strong absorption across the UV-visible region and excellent photothermal properties, achieving a significantly improved H_2 production rate of 136.9 μmol g^{-1} s^{-1} under illumination compared to the dark reaction condition, accompanied by an acetaldehyde selectivity of 82.8%. The E_a for H_2 production dramatically reduced from 78.3 kJ mol^{-1} in the dark to 51.8 kJ mol^{-1} under illumination, which demonstrates the function of incident light in facilitating the reaction kinetics. The wavelength-dependent catalytic activity confirms that the LSPR of Cu leads to enhanced surface reactions during light irradiation. FDTD simulation results further demonstrate the significant role of adjacent Pt NPs in enhancing the local electromagnetic field of Cu NPs to promote the ED reaction. This work provides an effective strategy to convert ethanol into hydrogen and high-value acetaldehyde under mild conditions.

4 Experimental section

4.1 Materials

Ethanol, acetaldehyde, $H_2PtCl_6{\cdot}6H_2O$, $Al(NO_3)_3{\cdot}9H_2O$, Na_2PdCl_4, $H_2IrCl_6{\cdot}6H_2O$, $AgNO_3$, and $HAuCl_4$ were purchased from Aladdin (Shanghai, China). $Cu(NO_3)_2{\cdot}3H_2O$, NaOH, and Na_2CO_3 were purchased from Macklin Chemical Reagent (Shanghai, China). CuO and Cu_2O were purchased from Sigma-Aldrich. There was no further purification treatment on all of the chemicals.

4.2 Synthesis of CuAl-LDH nanosheets

CuAl-LDH nanosheets with a Cu/Al molar ratio = 1 : 1 were synthesized *via* a coprecipitation reaction. Solution A was prepared by dissolving 1.21 g of $Cu(NO_3)_2{\cdot}3H_2O$ and 1.88 g of $Al(NO_3)_3{\cdot}9H_2O$ in 20 mL of deionized water. Solution B was prepared by dissolving NaOH (3.6 g) in deionized water (50 mL). Solution A and solution B were simultaneously dripped into a three-necked flask containing 180 mL of deionized water and 1.06 g Na_2CO_3 under constant stirring whilst maintaining a pH of 9.5. The resulting mixture was then heated at 65 °C for 4 h. The products were washed several times with deionized water until the pH of the supernatant was close to 7 and subsequently vacuum freeze-dried for 12 h.

4.3 Synthesis of *x* wt% M/CuAl-LDH nanosheets

100 mg of CuAl-LDH was dispersed into 20 mL of deionized water by ultrasonication. Then, a certain amount of $H_2PtCl_6{\cdot}6H_2O$ aqueous solution (10 mg mL^{-1} for Pt) was added to the above solution. The obtained solution was stirred for 12 h and then collected by centrifugation, washed several times with deionized water, and subsequently vacuum freeze-dried for 24 h. The synthetic methods of other samples were the same as above, except for changing the corresponding metal species. The obtained samples were named *x* wt% M/CuAl-LDH (*x* represents the metal weight loadings relative to CuAl-LDH,

M = Pt, Au, Ag, Pd, Ir, and Ag). 5 wt% M/CuAl-LDH was simply referred to as M/CuAl-LDH.

4.4 Preparation of *x* wt% LD-CuM and LD-Cu

The *x* wt% M/CuAl-LDH synthesized above were reduced in an H_2/Ar (10 : 90, v/v) stream at 500 °C for 2 h. The heating rate was 5 °C min^{-1}. After the reduction step, the products (denoted here as *x* wt% LD-CuM, where *x* representing the metal weight loadings relative to CuAl-LDH, M = Pt, Au, Ag, Pd, Ir, and Ag) were cooled to room temperature under a N2 atmosphere. 5 wt% LD-CuM was simply referred to as LD-CuM. CuAl-LDH was reduced using the same method and named LD-Cu.

4.5 Characterization

XRD patterns were obtained on a Bruker D8 Advance X-ray diffractometer equipped with a Cu Kα source (λ = 1.5405 Å) operating at 40 kV. TEM images were recorded on an HT-7700 (Hitachi, Japan) microscope operating at an accelerating voltage of 100 kV. HRTEM HAADF-STEM images and EDX elemental mapping images were acquired on an aberration-corrected JEM-ARM-300F (JEOL, Japan) microscope operating at 300 kV. XPS analyses were performed on an ESCALAB 250Xi X-ray photoelectron spectrometer equipped with a non-monochromatized Al Kα X-ray source. Inductively coupled plasma-optical emission spectroscopy (ICP-OES, Varian 710) was used to quantify the amounts of Al, Pt, and Cu in the samples. XAS measurements were performed at the Beijing Synchrotron Radiation Facility (Beamline 1W1B). The diffuse reflection spectra of the catalysts were measured using a UV-visible spectrophotometer on a Cary 7000 (Agilent) spectrometer with an integrating sphere attachment. Nitrogen adsorption/desorption isotherms were collected at 77 K on a Quadrasorb SI MP apparatus. Specific surface areas were calculated *via* the Brunauer–Emmett–Teller method.

4.6 Light-driven ED performance tests

Light-driven ED performance tests were conducted in a custom-built fixed-bed stainless steel flow reactor (volume = 56.0 mL) with a quartz window on the top for light irradiation. Typically, 5 mg photocatalyst was uniformly spread on a glass fiber membrane (Whatman, GE Healthcare Life Sciences, catalog number 1823-047) and then placed in the reactor (parallel to the quartz window). 50 mL min^{-1} Ar entered the reactor after passing through a bubbler containing ethanol. After purging for 30 min to remove the air in the reactor, a xenon light source (300 W xenon lamp, Beijing PerfectLight Technology Co., Ltd., PLSSXE-300D; 200 $< \lambda <$ 800 nm) was activated to drive the reaction. The reaction apparatus is shown in Fig. S6 of the ESI.† The gas products were quantified by withdrawing gas samples from the reactor and injecting them into a gas chromatograph (GC-2014C, Shimadzu Co., Ltd., Japan) equipped with an active-carbon-packed column and a thermal conductivity detector (TCD). The liquid products were detected and quantified by a GC (Shimadzu GC-2014) equipped with a flame ionization detector (FID) and an HP-5 column.

The catalyst membrane was supported by a quartz bowl to prevent direct contact with the stainless-steel reactor to reduce heat dissipation. A thermocouple was placed at the center of the catalyst membrane and in close contact with the catalyst to monitor the temperature of the catalyst.

E_a was calculated as:

$$K = A \cdot e^{\wedge}\left(-\frac{E_a}{RT}\right)$$

where K is the rate constant, A is the former factor, and T is the temperature. E_a is obtained by fitting the value of ln(r) at different temperatures (r represents H_2 production rate).

The apparent photoactivation efficiency (PAE) was calculated as:

$$\mathrm{PAE} = \frac{\Delta n E_a}{P_{light} t}$$

where Δn is the increase in the number of moles of H_2 produced under the photoactivated condition; P_{light} is the power of the incident light, t is the illumination time and E_a is the apparent activation energy in the dark condition.

The acetaldehyde selectivity is calculated according to the following equation:

$$\text{acetaldehyde selectivity (\%)} = \frac{2 \times n(\text{acetaldehyde})}{n(CH_4) + n(CO) + 2 \times n(\text{acetaldehyde})} \times 100\%$$

4.7 FDTD calculations

The computational simulation for the Al_2O_3-supported NPs with different shapes was performed using the FDTD method. The software package from FDTD Solutions (Lumerical Solutions, Inc.) with perfectly matched layer (PML) boundary conditions was employed to perform the 3D FDTD simulation. The mesh size was 0.02 nm, and the optical properties of Cu, Pt and Al_2O_3 were adopted from Palik data. The sizes of the Cu and Pt NPs were 30 nm and 3 nm, respectively, which were taken from the average values of the experimental size distribution. The interparticle gap between Cu NP and Pt NPs was 1 nm. A 500–600 nm plane-wave source along the z direction was used as the excitation source.

Data availability

The data supporting this article have been included as part of the ESI.†

Author contributions

Shihao Du: conceptualization, methodology, data curation, validation, writing – original draft. Run Shi: conceptualization, methodology, investigation, writing –

review & editing, supervision. Jiaqi Zhao: validation, investigation, writing – review & editing. Pu Wang: validation, investigation. Jinhu Wang: validation, investigation. Zhenhua Li: validation, investigation. Peng Miao: validation, investigation. Qianqian Shang: validation, investigation. Chi Duan: validation, investigation. Tierui Zhang: resources, project administration, funding acquisition.

Conflicts of interest

The authors declare that they have no known competing financial interests or personal relationships that could have appeared to influence the work reported in this paper.

Acknowledgements

The authors are grateful for financial support from the National Key R&D Program of China (2021YFA1500803), the National Natural Science Foundation of China (22421005, 52120105002, 52432006, 22272190, 22088102), the Beijing Natural Science Foundation (2222035), the CAS Project for Young Scientists in Basic Research (YSBR-004), the Young Elite Scientist Sponsorship Program by CAST (2021QNRC001), and the Youth Innovation Promotion Association of the CAS.

References

1 T. Takata, J. Jiang, Y. Sakata, M. Nakabayashi, N. Shibata, V. Nandal, K. Seki, T. Hisatomi and K. Domen, Photocatalytic water splitting with a quantum efficiency of almost unity, *Nature*, 2020, **581**, 411–414.

2 Y. Li, Y.-K. Peng, L. Hu, J. Zheng, D. Prabhakaran, S. Wu, T. J. Puchtler, M. Li, K.-Y. Wong, R. A. Taylor and S. C. E. Tsang, Photocatalytic water splitting by N- TiO_2 on MgO (111) with exceptional quantum efficiencies at elevated temperatures, *Nat. Commun.*, 2019, **10**, 4421.

3 D. Li, F. Xu, X. Tang, S. Dai, T. Pu, X. Liu, P. Tian, F. Xuan, Z. Xu, I. E. Wachs and M. Zhu, Induced activation of the commercial $Cu/ZnO/Al_2O_3$ catalyst for the steam reforming of methanol, *Nat. Catal.*, 2022, **5**, 99–108.

4 Y. Song, E. Ozdemir, S. Ramesh, A. Adishev, S. Subramanian, A. Harale, M. Albuali, B. A. Fadhel, A. Jamal, D. Moon, S. H. Choi and C. T. Yavuz, Dry reforming of methane by stable Ni–Mo nanocatalysts on single-crystalline MgO, *Science*, 2020, **367**, 777–781.

5 C. Palmer, D. C. Upham, S. Smart, M. J. Gordon, H. Metiu and E. W. McFarland, Dry reforming of methane catalysed by molten metal alloys, *Nat. Catal.*, 2020, **3**, 83–89.

6 Z. Li, J. Liu, J. Zhao, R. Shi, G. I. N. Waterhouse, X.-D. Wen and T. Zhang, Photo- driven hydrogen production from methanol and water using plasmonic Cu nanoparticles derived from layered double hydroxides, *Adv. Funct. Mater.*, 2023, **33**, 2213672.

7 J. Zhao, Y. Bai, Z. Li, J. Liu, W. Wang, P. Wang, B. Yang, R. Shi, G. I. N. Waterhouse, X.-D. Wen, Q. Dai and T. Zhang, Plasmonic Cu nanoparticles for the low-temperature photo-driven water-gas shift reaction, *Angew. Chem., Int. Ed.*, 2023, **62**, e202219299.

8 G. Giannakakis, P. Kress, K. Duanmu, H. T. Ngan, G. Yan, A. S. Hoffman, Z. Qi, A. Trimpalis, L. Annamalai, M. Ouyang, J. Liu, N. Eagan, J. Biener, D. Sokaras, M. Flytzani-Stephanopoulos, S. R. Bare, P. Sautet and E. C. H. Sykes, Mechanistic and electronic insights into a working NiAu single-atom alloy ethanol dehydrogenation catalyst, *J. Am. Chem. Soc.*, 2021, **143**, 21567–21579.

9 J. Yang, J. Zheng, C. Dun, L. J. Falling, Q. Zheng, J.-L. Chen, M. Zhang, N. R. Jaegers, C. Asokan, J. Guo, M. Salmeron, D. Prendergast, J. J. Urban, G. A. Somorjai, Y. Guo and J. Su, Unveiling highly sensitive active site in atomically dispersed gold catalysts for enhanced ethanol dehydrogenation, *Angew. Chem., Int. Ed.*, 2024, **63**, e202408894.

10 L. He, B.-C. Zhou, D.-H. Sun, W.-C. Li, W.-L. Lv, J. Wang, Y.-Q. Liang and A.-H. Lu, Catalytic conversion of ethanol to oxygen-containing value-added chemicals, *ACS Catal.*, 2023, **13**, 11291–11304.

11 D. A. Patel, G. Giannakakis, G. Yan, H. T. Ngan, P. Yu, R. T. Hannagan, P. L. Kress, J. Shan, P. Deshlahra, P. Sautet and E. C. H. Sykes, Mechanistic insights into nonoxidative ethanol dehydrogenation on NiCu single-atom alloys, *ACS Catal.*, 2023, **13**, 4290–4303.

12 Y. Wu, X. Zhu, S. Du, G. Huang, B. Zhou, Y. Lu, Y. Li, S. P. Jiang, L. Tao and S. Wang, Promoted hydrogen and acetaldehyde production from alcohol dehydrogenation enabled by electrochemical hydrogen pumps, *Proc. Natl. Acad. Sci. U. S. A.*, 2023, **120**, e2300625120.

13 V. Yadav, G. Sivakumar, V. Gupta and E. Balaraman, Recent advances in liquid organic hydrogen carriers: An alcohol-based hydrogen economy, *ACS Catal.*, 2021, **11**, 14712–14726.

14 S. Luo, H. Song, D. Philo, M. Oshikiri, T. Kako and J. Ye, Solar-driven production of hydrogen and acetaldehyde from ethanol on Ni-Cu bimetallic catalysts with solar-to-fuels conversion efficiency up to 3.8%, *Appl. Catal., B*, 2020, **272**, 118965.

15 J. Zhao, X. Guo, R. Shi, G. I. N. Waterhouse, X. Zhang, Q. Dai and T. Zhang, NiFe nanoalloys derived from layered double hydroxides for photothermal synergistic reforming of CH_4 with CO_2, *Adv. Funct. Mater.*, 2022, **32**, 2204056.

16 H. Xiong, Y. Dong, C. Hu, Y. Chen, H. Liu, R. Long, T. Kong and Y. Xiong, Highly efficient and selective light-driven dry reforming of methane by a carbon exchange mechanism, *J. Am. Chem. Soc.*, 2024, **146**, 9465–9475.

17 Z. Rao, K. Wang, Y. Cao, Y. Feng, Z. Huang, Y. Chen, S. Wei, L. Liu, Z. Gong, Y. Cui, L. Li, X. Tu, D. Ma and Y. Zhou, Light-reinforced key intermediate for anticoking to boost highly durable methane dry reforming over single atom Ni active sites on CeO_2, *J. Am. Chem. Soc.*, 2023, **145**, 24625–24635.

18 X. Xiong, C. Mao, Z. Yang, Q. Zhang, G. I. N. Waterhouse, L. Gu and T. Zhang, Photocatalytic CO_2 reduction to CO over Ni single atoms supported on defect-rich zirconia, *Adv. Energy Mater.*, 2020, **10**, 2002928.

19 J. Zhao, R. Shi, G. I. N. Waterhouse and T. Zhang, Selective photothermal CO_2 reduction to CO, CH_4, alkanes, alkenes over bimetallic alloy catalysts derived from layered double hydroxide nanosheets, *Nano Energy*, 2022, **102**, 107650.
20 H. Chen, Z. Li, C. Zhou, R. Shi and T. Zhang, Triphase photocatalytic water-gas-shift reaction for hydrogen production with enhanced interfacial diffusion at gas–liquid–solid interfaces, *Ind. Chem. Mater.*, 2024, **2**, 432–440.
21 Y. Wang, Y. Zhao, J. Liu, Z. Li, G. I. N. Waterhouse, R. Shi, X. Wen and T. Zhang, Manganese oxide modified nickel catalysts for photothermal CO hydrogenation to light olefins, *Adv. Energy Mater.*, 2020, **10**, 1902860.
22 X. Li, J. Pang, Y. Zhao, P. Wu, W. Yu, P. Yan, Y. Su and M. Zheng, Ethanol dehydrogenation to acetaldehyde over a $Cu^{\delta+}$-based Cu-MFI catalyst, *Chin. J. Catal.*, 2023, **49**, 91–101.
23 J. Pang, M. Yin, P. Wu, X. Li, H. Li, M. Zheng and T. Zhang, Advances in catalytic dehydrogenation of ethanol to acetaldehyde, *Green Chem.*, 2021, **23**, 7902–7916.
24 X. He, Y. Wang, X. Zhang, M. Dong, G. Wang, B. Zhang, Y. Niu, S. Yao, X. He and H. Liu, Controllable in situ surface restructuring of Cu catalysts and remarkable enhancement of their catalytic activity, *ACS Catal.*, 2019, **9**, 2213–2221.
25 V. Gombac, L. Sordelli, T. Montini, J. J. Delgado, A. Adamski, G. Adami, M. Cargnello, S. Bernal and P. Fornasiero, CuO_x-TiO_2 photocatalysts for H_2 production from ethanol and glycerol solutions, *J. Phys. Chem. A*, 2010, **114**(11), 3916–3925.
26 T. Montini, V. Gombac, L. Sordelli, J. J. Delgado, X. Chen, G. Adami and P. Fornasiero, Nanostructured Cu/TiO_2 photocatalysts for H_2 production from ethanol and glycerol aqueous solutions, *ChemCatChem*, 2011, **3**, 574–577.
27 C. Ampelli, R. Passalacqua, C. Genovese, S. Perathoner, G. Centi, T. Montini, V. Gombac, J. J. D. Jaenc and P. Fornasiero, H_2 production by selective photo-dehydrogenation of ethanol in gas and liquid phase on CuO_x/TiO_2 nanocomposites, *RSC Adv.*, 2013, **3**, 21776–21788.
28 S. Kim, J.-M. Kim, J.-E. Park and J.-M. Nam, Nonnoble-metal-based plasmonic nanomaterials: Recent advances and future perspectives, *Adv. Mater.*, 2018, **30**, 1704528.
29 U. Aslam, V. G. Rao, S. Chavez and S. Linic, Catalytic conversion of solar to chemical energy on plasmonic metal nanostructures, *Nat. Catal.*, 2018, **1**, 656–665.
30 G. Sharma, R. Verma, S. Masuda, K. M. Badawy, N. Singh, T. Tsukuda and V. Polshettiwar, Pt-doped Ru nanoparticles loaded on 'black gold' plasmonic nanoreactors as air stable reduction catalysts, *Nat. Commun.*, 2024, **15**, 713.
31 X. Zhang, S. Ju, C. Li, J. Hao, Y. Sun, X. Hu, W. Chen, J. Chen, L. He, G. Xia, F. Fang, D. Sun and X. Yu, Atomic reconstruction for realizing stable solar-driven reversible hydrogen storage of magnesium hydride, *Nat. Commun.*, 2024, **15**, 2815.
32 S. Luo, H. Lin, Q. Wang, X. Ren, D. Hernández-Pinilla, T. Nagao, Y. Xie, G. Yang, S. Li, H. Song, M. Oshikiri and J. Ye, Triggering water and methanol activation for solar-driven H_2 production: Interplay of dual active sites over plasmonic ZnCu alloy, *J. Am. Chem. Soc.*, 2021, **143**, 12145–12153.
33 M. Herran, A. Sousa-Castillo, C. Fan, S. Lee, W. Xie, M. Döblinger, B. Auguié and E. Cortés, Tailoring plasmonic bimetallic nanocatalysts toward sunlight-driven H_2 production, *Adv. Funct. Mater.*, 2022, **32**, 2203418.
34 H. Jin, M. Herran, E. Cortés and J. Lischner, Theory of hot-carrier generation in bimetallic plasmonic catalysts, *ACS Photonics*, 2023, **10**, 3629–3636.
35 W. Jiang, B. Q. L. Low, R. Long, J. Low, H. L. Y. Tang, C. H. T. Chai, H. Zhu, H. Zhu, Z. Li, X. J. Loh, Y. Xiong and E. Ye, Active site engineering on plasmonic nanostructures for efficient photocatalysis, *ACS Nano*, 2023, **17**, 4193–4229.
36 M. Herran, S. Juergensen, M. Kessens, D. Hoeing, A. Köppen, A. Sousa-Castillo, W. J. Parak, H. Lange, S. Reich, F. Schulz and E. Cortés, Plasmonic bimetallic two- dimensional supercrystals for H_2 generation, *Nat. Catal.*, 2023, **6**, 1205–1214.
37 P. Gao, L. Zhong, L. Zhang, H. Wang, N. Zhao, W. Wei and Y. Sun, Yttrium oxide modified $Cu/ZnO/Al_2O_3$ catalysts via hydrotalcite-like precursors for CO_2 hydrogenation to methanol, *Catal. Sci. Technol.*, 2015, **5**, 4365–4377.
38 T. Chen, S. Xu, T. Zhao, X. Zhou, J. Hu, X. Xu, C. Liang, M. Liu and W. Ding, Accelerating ethanol complete electrooxidation via introducing ethylene as the precursor for the C–C bond splitting, *Angew. Chem., Int. Ed.*, 2023, **62**, e202308057.
39 L. Li, S. Miyazaki, S. Yasumura, K. W. Ting, T. Toyao, Z. Maeno and K. Shimizu, Continuous CO_2 capture and selective hydrogenation to CO over Na-Promoted Pt nanoparticles on Al_2O_3, *ACS Catal.*, 2022, **12**, 2639–2650.
40 Y. Shundo, T. T. Nguyen, S. Akrami, P. Edalati, Y. Itagoe, T. Ishihara, M. Arita, Q. Guo, M. Fuji and K. Edalati, Oxygen vacancy-rich high-pressure rocksalt phase of zinc oxide for enhanced photocatalytic hydrogen evolution, *J. Colloid Interface Sci.*, 2024, **666**, 22–34.
41 M. Katai, P. Edalati, J. H.-Jimenez, Y. Shundo, T. Akbay, T. Ishihara, M. Arita, M. Fuji and K. Edalati, Black brookite rich in oxygen vacancies as an active photocatalyst for CO_2 conversion: experiments and first-principles calculations, *J. Photochem. Photobiol., A*, 2024, **449**, 115409.
42 X. Bian, Y. Zhao, C. Zhou and T. Zhang, Minimizing temperature bias through reliable temperature determination in gas-solid photothermal catalytic reactions, *Angew. Chem., Int. Ed.*, 2023, **62**, e202219340.
43 L. Mascaretti, A. Schirato, T. Montini, A. Alabastri, A. Naldoni and P. Fornasiero, Challenges in temperature measurements in gas-phase photothermal catalysis, *Joule*, 2022, **6**, 1727–1732.
44 J. Yang, J. Zheng, C. Dun, L. J. Falling, Q. Zheng, J.-L. Chen, M. Zhang, N. R. Jaegers, C. Asokan, J. Guo, M. Salmeron, D. Prendergast, J. J. Urban, G. A. Somorjai, Y. Guo and J. Su, Unveiling highly sensitive active site in atomically dispersed gold catalysts for enhanced ethanol dehydrogenation, *Angew. Chem.*, 2024, **65**, e202408894.
45 Y. Zhang, H. Hu, Z. Yang, S. Liu, T. Yang, L. Wang, Y. Sun, X. Wang, Q. Li and P. Tian, Spatial confinement effect of zeolite Silicalite-1 on dispersing high loading Cu

nanoparticles and their superior ethanol dehydrogenation catalytic performance, *Appl. Catal., B*, 2025, **367**, 125099.

46 X. Guo, W. Ye, Z. Chen, A. Zhou, D. Jin and T. Ma, Simulated solar light-driven photothermal preferential oxidation of carbon monoxide in H_2-rich streams over fast-synthesized CuCeO2–x nanorods, *Appl. Catal., B*, 2022, **310**, 121334.

47 Y. Xin, K. Yu, L. Zhang, Y. Yang, H. Yuan, H. Li, L. Wang and J. Zeng, Copper- based plasmonic catalysis: Recent advances and future perspectives, *Adv. Mater.*, 2021, **33**, 2008145.

48 S. Linic, U. Aslam, C. Boerigter and M. Morabito, Photochemical transformations on plasmonic metal nanoparticles, *Nat. Mater.*, 2015, **14**, 567–576.

49 A. Naldoni, F. Riboni, U. Guler, A. Boltasseva, V. M. Shalaev and A. V. Kildishev, Solar-powered plasmon-enhanced heterogeneous catalysis, *Nanophotonics*, 2016, **5**, 112–133.

50 C. Kim, B. L. Suh, H. Yun, J. Kim and H. Lee, Surface plasmon aided ethanol hydrogenation using Ag–Ni binary nanoparticles, *ACS Catal.*, 2017, **7**, 2294–2302.